RESEARCH ARTICLE
PLANETARY SCIENCES

Earth and Planetary Physics
9: 891–903, 2025
doi: 10.26464/epp2025021

Statistical properties of hot flow anomalies around Mars

MingYu Wu[1,2*], HeYin Wang[1], Lei Wang[1], GuoQiang Wang[1], SuDong Xiao[1], YangJun Chen[1], Qi Lü[1], Peng E[3], AiMin Du[6], and TieLong Zhang[1,4,5*]

[1]Shenzhen Key Laboratory of Numerical Prediction for Space Storm, Harbin Institute of Technology, Shenzhen 518055, China;

[2]Key Laboratory of Solar Activity and Space Weather, National Space Science Center, Chinese Academy of Sciences, Beijing 100190, China;

[3]Harbin Institute of Technology, Harbin 150001, China;

[4]State Key Laboratory of Lunar and Planetary Sciences, Macau University of Science and Technology, Macao 999078, China;

[5]Space Research Institute, Austrian Academy of Sciences, Graz 8042, Austria;

[6]Institute of Geology and Geophysics, Chinese Academy of Sciences, Beijing 100029, China

Key Points:

- HFAs (Hot flow anomalies) can be found in a wide region from the dayside to the terminator region of Mars.
- HFAs around Mars occur most preferentially with high-speed solar wind.
- HFAs around Mars can lead to variations in solar wind dynamic pressure by factors of 10.

Citation: Wu, M. Y., Wang, H. Y., Wang, L., Wang, G. Q., Xiao, S. D., Chen, Y. J., Lü, Q., E, P., Du, A. M., and Zhang, T. L. (2025). Statistical properties of hot flow anomalies around Mars. *Earth Planet. Phys.*, *9*(4), 891–903. http://doi.org/10.26464/epp2025021

Abstract: Hot flow anomalies (HFAs) are not only a terrestrial phenomenon, but also a solar-system-wide phenomenon, one that can cause significant perturbations in planetary magnetospheres and ionospheres. In this study, based on the observations of Mars Atmosphere and Volatile EvolutioN (MAVEN) mission in the region upstream of the Martian bow shock from the year 2014 to 2020, we have investigated the statistical properties of HFAs around Mars. Our results show that HFAs can be found in a wide region of Mars, from the dayside to the terminator region. On average, these HFAs last 63 seconds, with a thickness of 28 local proton gyroradii. They are more prevalent when the ambient solar wind is denser and faster, and usually occur when the interplanetary magnetic field magnitude is between 1–4 nT. Martian HFAs can also lead to solar wind dynamics multiplying in pressure by factors of ten within only tens of seconds, which could significantly influence the heights of the Martian ionopause and induced magnetosphere boundary. By comparing HFAs around Earth, we suggest that these phenomena are primarily governed by solar wind dynamics rather than local planetary conditions.

Keywords: magnetic fields; Mars; solar wind; hot flow anomaly

1. Introduction

In our solar system, planetary bow shocks are considered to play a key role in solar wind–planet interaction. The pristine solar wind first undergoes compression at the bow shock, resulting in 'shocked' solar wind with pronounced temporal and spatial fluctuations that can directly influence the magnetospheres of both magnetized and unmagnetized planets (e.g., Axford, 1962; Dubinin et al., 1998; Vignes et al., 2002; Zhang TL et al., 2008). During this process, many transient structures upstream of the planetary bow shock may arise and subsequently disturb the magnetosphere–ionosphere system (e.g., Sibeck et al., 1999; Zhang H et al., 2010). Among these transient structures, the hot flow anomaly (HFA) is the most extensively studied (Schwartz et al., 1985, 2000; Thomsen et al., 1986; Zhang H et al., 2010; Zhao LL et al., 2015).

Correspondence to: M. Y. Wu, wumingyu@hit.edu.cn
T. L. Zhang, tielong.zhang@oeaw.ac.at
Received 13 DEC 2024; Accepted 06 FEB 2025.
First Published online 28 FEB 2025.

HFAs were firstly discovered in the foreshock region of the terrestrial bow shock (Schwartz et al., 1985). Their most noticeable feature is a magnetic cavity which is flanked by the magnetic field and plasma compression on one or both sides (e.g., Thomsen et al., 1986; Sibeck et al., 1999; Facskó et al., 2009; Zhang H et al., 2010). Inside this magnetic cavity, ions are notably hotter and more tenuous compared to the ambient solar wind, while the corresponding bulk flow velocity towards the sun–planet direction experiences a significant reduction (e.g., Wang S et al. 2013a, b). Upstream of Earth, these HFAs can persist with durations ranging from seconds to minutes, with an occurrence rate of approximately 2–3 events per day (Schwartz et al., 2000; Facskó et al., 2009). Remarkably, these HFAs often originate on the dayside and then propagate tens of Earth radii towards the mid-tail region at the nightside (Liu TZ et al., 2020b).

Global simulations have already demonstrated that HFAs are typically formed during the connection of the interplanetary current sheet to the planetary bow shock (Lin Y, 2002; Omidi and Sibeck, 2007; Lin Y et al., 2022). If the solar wind motional electric field points to the current sheet on at least one side, reflected ions from the bow shock are channeled back along the current sheet, and heated due to the coupling between the reflected ions and ions in the current sheet (Onsager et al., 1991; Thomas et al., 1991). In this process, a hot core region is produced, and then it can expand and compress the surrounding solar wind, leading to the compression regions at the edge of this current sheet (Lin Y, 2002; Omidi and Sibeck, 2007). This generation mechanism has suggested that HFAs should form wherever there is an interaction between an interplanetary current sheet and a collisionless shock under an appropriate condition. Therefore, they should be widespread phenomena around planetary bow shocks in the solar system. Nowadays, HFAs have already been observed at Mercury (Uritsky et al., 2014), Venus (Slavin et al., 2009; Collinson et al., 2012, 2014), Mars (Collinson et al., 2015), Jupiter (Valek et al., 2017), and Saturn (Masters et al., 2009). Some similar features of HFAs are detected at upstream regions of these planets' bow shock, but the typical size and occurrence rate of HFAs around these planets have large distinctions (Masters et al., 2009; Collinson et al., 2014; Uritsky et al., 2014).

Although Mars is an unmagnetized planet without an interior magnetic field, its foreshock region remains abundant in various waves and transient structures, which could be driven by reflected ions from the bow shock or newly born ions from Mars (e.g., Russell and Hoppe, 1983; Mazelle et al., 2004; Eastwood et al., 2005). Øieroset et al. (2001) presented observations from the Mars Global Surveyor (MGS) of HFA-like magnetic field configurations and electron signatures upstream of the Martian bow shock. However, owing to the lack of ion measurements due to the absence of an ion detector on MGS, these signatures cannot be definitively classified as HFAs. Following the launch of NASA's Mars Atmosphere and Volatile EvolutioN (MAVEN) mission (Jakosky et al., 2015), the simultaneous high-resolution ion, electron, and magnetic field data are available for the study of HFAs around Mars for the first time. Based on the measurements by MAVEN, Collinson et al. (2015) reported an HFA event in the Martian foreshock region. This HFA exhibits relatively weaker ion perturbations compared to those observed near the terrestrial bow shock, but this event also has the potential to change the height of the Martian ionopause.

While previous studies have confirmed the existence of Martian HFAs, this study utilizes simultaneous magnetic field and particle measurements from MAVEN to obtain the general properties of HFAs around Mars, and compares their features with results from terrestrial HFAs. Additionally, there are also several statistical studies of HFAs around non-Earth planets like Mercury (Uritsky et al., 2014), Venus (e.g., Collinson et al., 2014), and Saturn (Masters et al., 2009), but these works typically lack ion measurements due to limitations in payload accuracy and observation duration. Therefore, our results can also serve as a valuable reference for a better understanding of the question of how varying solar wind conditions modify the interaction between interplanetary discontinuities and planetary bow shocks.

In this study, we have conducted a comprehensive analysis of the properties of HFAs by examining MAVEN data captured upstream of the Martian bow shock. In Section 2, we introduce the MAVEN data utilized for this research and establish the criteria for selecting Martian HFA events. Section 3 presents a case study of the selected HFA events around Mars, followed by Section 4, which highlights the statistical properties of these Martian HFAs. In Section 5, we compare our findings with the characteristics of HFAs upstream of Earth. Additionally, we discuss the potential effects of Martian HFAs on the ionosphere and induced magnetosphere of Mars. Finally, Section 6 summarizes the key results of our investigation.

2. Data Set

The MAVEN mission consists of a single orbiter observing how the solar wind interacts with the Martian upper atmosphere (Jakosky et al., 2015). MAVEN entered orbit around Mars on September 21, 2014, and began its primary scientific investigations in the same year. It initially had an elliptical orbit of 150 km × 6200 km; by May of 2019, it reached a new orbit of 150 km × 4500 km. The inclination angle and period of MAVEN's orbit are 74° and 4.5 h, respectively. MAVEN is equipped with a particles and fields package, which can carry out comprehensive measurements of the solar wind and induced magnetosphere. Such orbit and payload offer an opportunity to investigate the foreshock transients upstream of the Martian bow shock.

The Magnetometer (MAG) consists of two independent fluxgate magnetometer sensors that can provide 32 Hz magnetic field vector data dynamic range up to 65,365 nT per axis (Connerney et al., 2015). Meanwhile, the Solar Wind Ion Analyzer (SWIA) (Halekas et al., 2015) can supply the solar wind ion data with a time resolution of 4 s, covering an energy range from 25 eV to 25 keV. It should be noted that SWIA does not discriminate between ion species. All ions are assumed to be protons during the calculation of moments (ion density, velocity, and temperature) by SWIA measurements. In the cases of computed density and velocity, such an assumption is usually a good approximation of the solar wind which typically consists of more than 90% protons. However, the newly born ion population can sometimes lead to an artificially raised temperature (Halekas et al., 2017), e.g., pickup protons from Mars sometimes represent a source of ions upstream of the Martian bow shock (Yamauchi et al., 2015; Rahmati et al., 2017). Therefore, SWIA onboard-computed solar wind temperature moments are not used for quantitative analysis in this study. The other instrument named as Suprathermal and Thermal Ion Composition (STATIC) analyzer (McFadden et al., 2015) onboard MAVEN can provide ion mass compositions with time resolutions of 4–128 s, in the energy range of 0.1 eV–30 keV. Since STATIC can saturate in the intense solar wind, in this study the SWIA measurements are mainly used to obtain the solar wind parameters. The STATIC data are only used to verify the density ratio between protons and heavy ions from Mars, which can ensure the validity of the SWIA moments data.

In this study, we employ magnetic field and ion measurements in the vicinity of the Martian bow shock to identify HFAs around Mars. Unless specified otherwise, the aforementioned data are referenced to the right-handed Mars Solar Orbital (MSO) coordinate system, which is centered on Mars. In this system, the positive X axis points toward the Sun, the Z axis points along Martian orbital momentum, and the Y axis completes the right-handed orientation of the coordinate system.

For the selection of potential Martian HFA candidates, we quantify the criteria based on previous terrestrial HFAs studies (e.g., Schwartz et al., 2000; Facskó et al., 2009; Zhao LL et al., 2015) that were: (1) a reduction in the magnitude of magnetic field and ion number density within the HFA core exceeding 10% of ambient values, calculated as the one-minute average outside the event; (2) a rotation in magnetic field direction across the HFA event greater than 30°, indicating the presence of a distinct current sheet; (3) inside the HFA core region, an increase in ion temperature inferred from the ion energy spectra, accompanied by a decrease in bulk velocity along the Sun–Mars axis; (4) compression regions flanking the HFA events, exhibiting enhanced magnetic field magnitude and ion density. Moreover, interactions between pristine solar wind and the Martian bow shock often generate upstream perturbations of considerable amplitude. Following the guidelines proposed by Halekas et al. (2017), these perturbations, characterized by fluctuations in solar wind density and magnetic field magnitude, can be categorized into two types: isolated events and repeated events. Isolated events are defined as those that occur without any preceding or succeeding upstream events within a 10-minute window, while repeated events constitute a series of events with a duration shorter than 10 minutes. To reduce the uncertainty in solar wind parameter values associated with repeated events due to their transient nature, we have confined our analysis to isolated HFA events. Based on these rigorous criteria, we have selected a total of 60 HFA events as the basis for a statistical analysis of HFA properties around Mars, as shown in Table 1.

Table 1. The intervals where MAVEN encountered a Martian HFA event. For each event, the rotation angle of magnetic field across the HFA, the minimum values of magnetic field magnitude B_{min} and ion number density N_{core} from SWIA are also listed.

Event	Date	Start	End	Rotation angle (°)	B_{min} (nT)	N_{core} (cm^{-3})
1	2014/11/14	18:58	19:13	89	1.58	0.47
2	2014/12/2	1:33	1:48	38	0.5	0.1
3	2014/12/2	5:40	5:55	42	0.87	0.27
4	2015/2/28	23:00	23:15	103	03	0.08
5	2015/3/2	7:12	7:27	62	0.6	0.76
6	2015/7/19	19:18	19:33	144	0.14	0.01
7	2015/8/16	2:35	2:50	34	1.14	0.13
8	2015/8/23	20:20	20:35	56	0.43	0.01
9	2015/8/25	17:55	18:10	73	0.09	0.13
10	2015/9/10	2:41	2:56	67	0.48	0.27
11	2015/9/11	15:30	15:45	66	0.55	0.01
12	2016/2/11	8:25	8:40	43	0.39	0.07
13	2016/2/24	2:45	3:00	47	0.75	0.41
14	2016/3/9	5:24	5:39	171	0.45	0.33
15	2016/6/14	11:51	12:06	35	2.26	0.19
16	2016/6/15	17:48	18:03	43	1.43	0.56
17	2016/6/20	8:31	8:46	145	0.14	0.39
18	2016/7/6	7:46	8:01	47	0.45	0.10

Continued from Table 1

Event	Date	Start	End	Rotation angle (°)	B_{min} (nT)	N_{core} (cm^{-3})
19	2016/7/15	18:50	19:05	50	0.17	0.02
20	2016/8/5	14:51	15:06	43	1.11	0.46
21	2016/8/13	1:05	1:20	49	0.32	0.29
22	2016/8/25	14:24	14:39	76	0.54	0.26
23	2016/8/29	22:29	22:44	33	0.73	0.43
24	2016/9/2	13:46	14:01	51	0.66	0.28
25	2016/9/25	13:00	13:15	35	1.07	1.49
26	2016/9/26	7:06	7:21	73	2.20	1.59
27	2016/10/1	21:25	21:40	42	0.79	0.43
28	2016/12/19	9:49	10:04	82	0.67	0.73
29	2016/12/23	0:41	0:56	86	0.43	0.04
30	2016/12/29	8:24	8:39	169	0.40	0.95
31	2016/12/30	12:44	12:59	154	0.53	1.38
32	2017/1/2	8:32	8:47	64	1.58	0.58
33	2017/1/24	8:24	8:39	103	0.42	0.18
34	2017/1/28	10:28	10:43	60	0.40	0.05
35	2017/1/30	11:43	11:58	91	0.95	0.63
36	2017/2/6	3:10	3:25	88	0.28	0.36
37	2017/7/12	22:38	22:53	40	0.70	0.08
38	2017/7/20	6:34	6:49	143	1.20	1.81
39	2017/7/20	20:29	20:44	78	1.20	1.81
40	2018/1/17	13:31	13:46	99	0.67	0.69
41	2018/1/18	13:26	13:41	124	0.81	0.86
42	2018/2/4	18:21	18:36	103	0.25	0.49
43	2018/4/6	8:41	8:56	46	0.60	0.04
44	2018/4/22	9:24	9:39	171	0.26	0.12
45	2018/7/23	14:08	14:23	58	0.91	0.04
46	2018/7/26	12:50	13:05	71	0.25	0.48
47	2018/8/12	8:12	8:27	64	0.51	1.06
48	2018/8/17	9:28	9:43	137	0.35	0.11
49	2018/9/20	0:42	0:57	35	0.06	0.00
50	2018/9/20	22:58	23:13	42	0.79	0.36
51	2018/9/23	3:19	3:34	52	0.46	0.07
52	2018/10/1	5:23	5:38	95	0.22	0.03
53	2018/10/14	14:47	15:02	69	0.70	0.04
54	2018/12/25	7:13	7:28	110	0.43	0.09
55	2019/2/16	23:51	00:06 (+1 day)	126	0.19	0.10
56	2019/2/24	22:28	22:43	59	0.73	0.17
57	2019/6/22	2:11	2:26	42	0.35	0.03
58	2019/8/1	17:37	17:52	45	0.33	0.01
59	2019/8/9	8:50	9:05	48	0.77	0.17
60	2020/8/5	20:52	1:07	75	1.92	0.22

3. An HFA Event on October 1, 2018

This paper begins by analyzing a representative HFA event detected near Mars, based on measurements from MAVEN. Subsequently, this study explores the statistical properties of HFAs situated upstream of the Martian bow shock.

Figure 1 presents a representative HFA event near Mars that is illustrative of our investigation. This event was observed at about 05:31 on October 1, 2018, when MAVEN was located upstream of the Martian bow shock. From the top to the bottom of Figure 1, there are (a) the three magnetic field components; B_x (dark blue line), B_y (light green line), and B_z (red line) in MSO frame; (b) the total magnetic field intensity B_T; (c) the shock normal angle θ_{Bn} which is the angle between the upstream IMF to the model-predicted Martian bow shock surface normal (using the bow shock model of Trotignon et al. (2006)); (d) the solar wind speed V_T (black line), and the magnitude of bulk velocity component V_x along the Mars–Sun direction (dark blue line); (e) the ion density N_i obtained by SWIA (black line) and the hydrogen density N_{H^+} obtained by STATIC (light green line); (f) the densities of N_{O^+} (black line) and $N_{O_2^+}$ (light green line) obtained by STATIC; (g) the ratio $N_{H^+}/\left(N_{O^+}+N_{O_2^+}\right)$; (h) the solar wind dynamic pressure P_{dyn}; and (i) the solar wind ion spectrogram from SWIA.

Throughout the time interval shown in Figure 1, MAVEN was in the solar wind, which can be easily identified by the ion spectrum from SWIA. During the interval of 05:30:30 UT to 05:32:30 UT, a magnetic cavity accompanied by strong ion density depletion and ion heating was detected by MAVEN. The two sides of this cavity are magnetic field and plasma compression regions. We denote the 1-minutes duration before and after the cavity as 'pre' and 'post', respectively. The mean IMF in the 'pre' interval ($\boldsymbol{B}_{pre}$) is (−1.3, 1.2, 1.0) nT, and the mean IMF in the 'post' interval ($\boldsymbol{B}_{post}$) is (−1.0, −1.6, 0.3) nT. Hence, this transition accompanies with a substantial 95° rotation of the IMF orientation, implicating the involvement of a current sheet in the observed magnetic cavity's formation. All these features demonstrate that this magnetic cavity, flanked by magnetic field and ion density enhancements, is an HFA event. Consistent with terrestrial HFAs, the core of Martian HFAs can also be characterized by a drop in magnetic field magnitude and ion density below their ambient values. In the core of our event marked by the yellow horizontal bar, B_T is about 2–3 times smaller than the ambient IMF values. The two compression regions of HFA are marked by the black horizontal bars, which are identified by the increase of ion density (hydrogen density N_{H^+}) and magnetic field magnitude B_T.

Based on the bow shock model (Trotignon et al., 2006), we are able to compute the shock normal angle θ_{Bn} in relation to the IMF. The bow shock normal is calculated at the point of intersection where a magnetic field line passes through the spacecraft. Prior to the HFA event, θ_{Bn} is estimated at approximately 150°, which means MAVEN was located at the upstream of a quasi-parallel shock. The presence of weak magnetic fluctuations and ultra-low frequency (ULF) waves are also observed in this region, which can be taken as indicators of the foreshock. After the HFA, the upstream interplanetary magnetic field does not intersect with the modeled bow shock, so it is not possible to calculate the corresponding shock normal angle θ_{Bn}. In such a case, it can be inferred that MAVEN is located at the upstream of a quasi-perpendicular shock. Both the IMF and the solar wind are highly stable during the period after this HFA event, which is additional evidence of being located upstream of a quasi-perpendicular shock. Throughout these observations, the HFA event appears to locate at the transitional boundary demarcating the shift from a quasi-parallel to a quasi-perpendicular shock regime.

On October 1, 2018, Mars was located around the perihelion, and the solar activity was very low. Liu D et al. (2021) have presented the statistical properties of solar wind upstream of Mars. From their Table 1, the average solar wind speed is 353 km/s when Mars is near perihelion under low solar activity (Liu D et al., 2021). In this event, the ambient solar wind speed is about 380 km/s, which is slightly faster than average.

Panels (e), (f), and (g) provide the details of ions in this event. Contrary to conditions encountered in the vicinity of Earth, it may be assumed that ions originating from Mars are non negligible within the solar wind environment upstream of the bow shock (Mazelle et al., 2004). In this HFA event, the density of heavy ions in the Martian exosphere reaches a noteworthy level. $N_{O_2^+}$ is only slightly higher than N_{O^+}, but N_{H^+} is about 15 times higher than $N_{O_2^+}$ or N_{O^+}. Therefore, in this event, protons are still the dominant ion species in the solar wind. The ion density values derived from SWIA closely align with N_{H^+} obtained by STATIC measurements. The congruence in temporal trends between these two independent sets of number densities lends further credence to the reliability of SWIA-derived ion densities in HFA studies.

Regarding heavy ions from Mars and their potential impact within HFAs, observations indicate that they can be effectively disregarded. Typically, the ratio of proton density to heavy ion density exceeds one hundred in the core region of this HFA, representing a magnitude significantly higher than the typical ratio observed in the ambient solar wind. This finding proves the interaction of solar wind protons and shock-reflected protons as the dominant factors within the HFA, while the dynamics of heavy ions are seemingly unimportant for the formation of HFA. Halekas et al. (2017) found that planetary ions do not exert a predominant influence on the generation of strong upstream waves in the foreshock region. Instead, it appears that shock-reflected protons upstream of the Martian bow shock play a key role in the higher amplitude fluctuations and structural characteristics associated with HFAs. Consequently, it can be expected that the mechanisms underlying the generation of HFAs in the Martian environment could be the same as those in the vicinity of Earth.

4. A Survey of Martian HFAs

In this study, the magnetic field and ion parameters of HFAs are obtained by the MAG and SWIA measurements in the core region of these HFAs, while the averaged field and plasma parameters outside of HFAs are taken as the ambient IMF and solar wind conditions. For all selected 60 HFA events, similar magnetic cavity and compression boundaries are encountered by MAVEN. All these events are linked to current sheets, which are identified by the large rotation of IMF crossing HFAs.

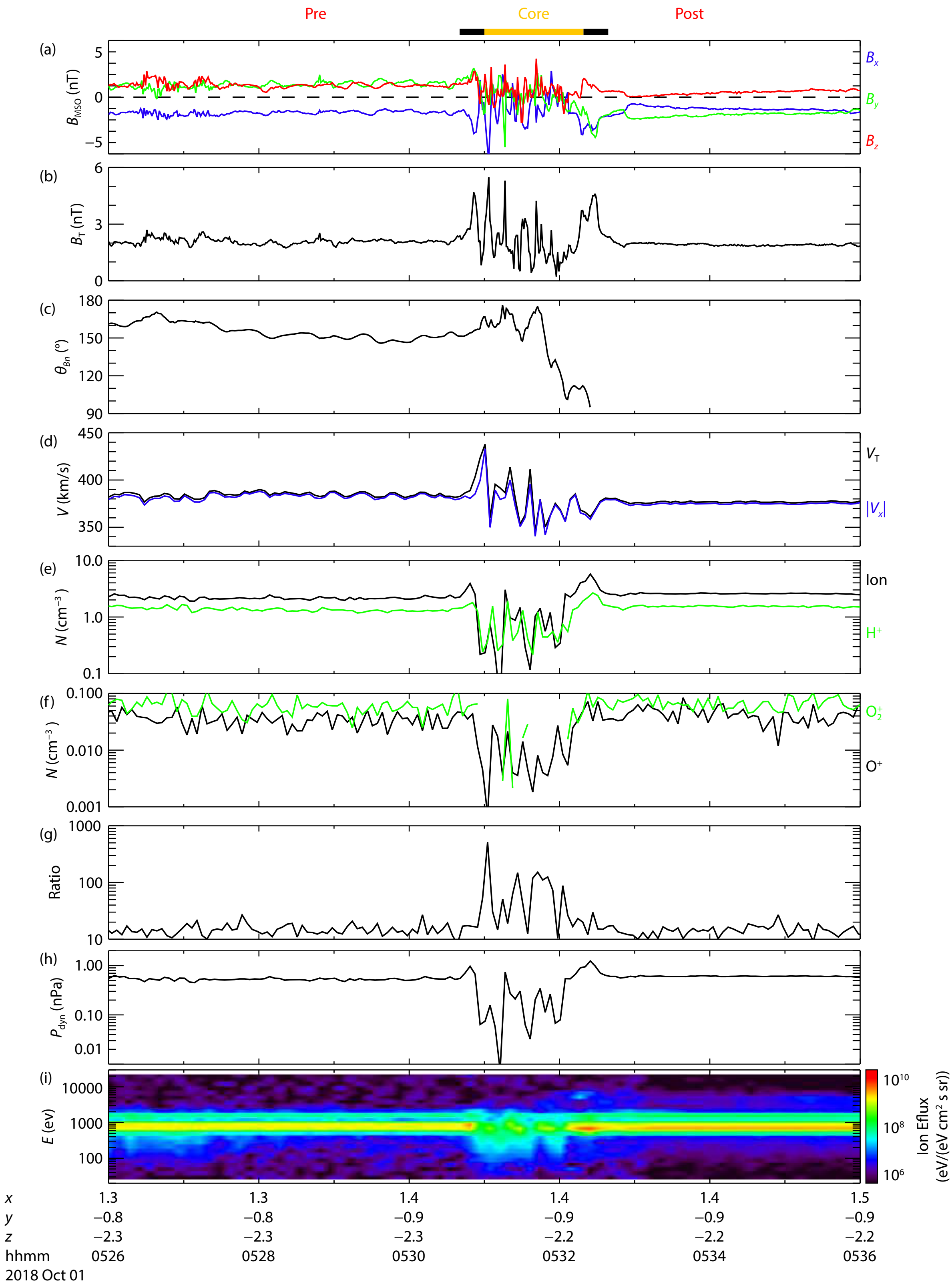

Figure 1. Overview of the HFA event on October 1, 2018, with magnetic field and bulk velocity in MSO coordinate system. From top to bottom: (a) three components of the magnetic field; (b) magnetic field magnitude; (c) shock normal angle of the magnetic field vector to the model-predicted Martian bow shock surface normal; (d) the speed of solar wind (black line) and the magnitude of the x component of solar wind velocity obtained by SWIA (blue line); (e) ion number density from SWIA (black line) and hydrogen number density from STATIC (light green line); (f) the number densities of monovalent oxygen ion (black line) and monovalent dioxygen ion (light green line) from STATIC; (g) the density ratio $N_{H^+}/\left(N_{O^+}+N_{O_2^+}\right)$; (h) the solar wind dynamic pressure P_{dyn}; and (i) the solar wind ion spectrogram from SWIA. The core region of this HFA is marked by a horizontal yellow bar, and the compression regions on the two sides of this core are marked by horizontal black bars.

4.1 Locations of HFA Events

Because of the large rotation angle of ambient IMF around HFAs, this distribution is difficult to represent in the Mars Solar Electrical (MSE) coordinate system. Figure 2 displays the spatial distribution of all the selected HFA events encountered in proximity to Mars, respectively in the (a) X–R (where $R = \sqrt{Y^2 + Z^2}$) and (b) Y–Z planes in the MSO frame. The unit of each axis is the Martian radius (R_M). The black solid and dash curves represent the modeled locations of the Martian bow shock and induced magnetosphere boundary, respectively (Trotignon et al., 2006). HFAs can be clearly observed both at dayside and terminator regions. Due to limitations in the orbital coverage of MAVEN, there is almost no observation in the foreshock region at nightside. This precludes the identification of HFA events occurring at the nightside in the present study.

In Figure 2b, a total of 25 HFA events are observed in the southern hemisphere, while 35 HFA events are observed in the northern hemisphere. The spatial distribution of our HFA events exhibits a south–north asymmetry. The Martian bow shock is a three-dimensional structure with a south–north asymmetry controlled by the upstream solar wind parameters (e.g. the solar wind dynamic pressure and the interplanetary magnetic field) and the downstream planetary conditions (e.g., the crustal magnetic field and the ionosphere) (Gruesbeck et al., 2018; Wang M et al., 2020). Such a spatial distribution of HFAs could be related to the three-dimensional shape of the bow shock.

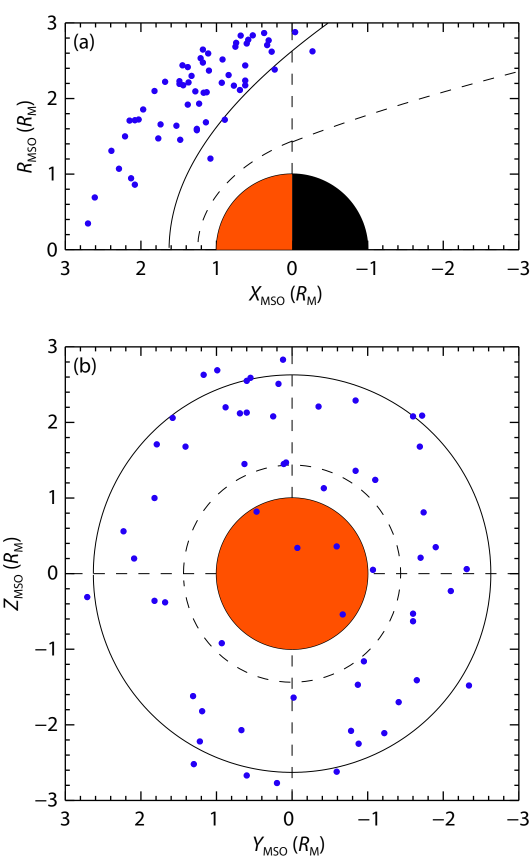

Figure 2. The projection of positions of HFA events around Mars in the (a) X–R and (b) Y–Z planes of the MSO frame, where $R = \sqrt{X^2 + Y^2}$. The dark blue dots are the observed positions of Martian HFA events. The solid and dashed curves are the modeled bow shock and induced magnetosphere boundary, respectively (Trotignon et al., 2006).

4.2 Duration and Size of HFAs

Figure 3 shows the histograms of various parameters of HFA events, including (a) the temporal duration of events, (b) the rotation angle of magnetic field across HFAs (θ_B), (c) the spatial extent of events in units of R_M, and (d) the spatial extent of events in units of local proton gyroradii (R_P). As shown in Figure 1, the Martian HFA also has a hot and tenuous core region of a kind that is also observed in other planets (Facskó et al., 2009; Valek et al., 2017). In this study, we take the duration of the core region of each HFA event as representative of the duration of HFAs. The duration of HFAs around Mars varies from 12 s to 164 s, and the most probable duration is about 60 s. The average duration of HFAs is 63 ± 39 s.

The rotation angle θ_B is calculated by the ambient IMF preceding and succeeding an HFA event. In the selection of HFA events, we use the criteria $\theta_B > 30°$ to exclude the spontaneous hot flow anomaly (SHFA) events which are formed by the nonlinear evolution of ULF waves in the foreshock (Collinson et al., 2017). As shown in Figure 3b, the occurrence rate of HFA events clearly decreases according to an increase of the rotation angle θ_B. The average θ_B is 76° ± 39°.

According to Equation (1), we can estimate the normal direction of HFA events using the mean magnetic field outside of these HFAs. This enables the calculations of the flow velocity in the normal direction, which, in conjunction with the solar wind velocity's normal component and the event duration, permits the estimation of the spatial scale of HFAs. Figures 3c and d illustrate the thickness of HFAs, normalized by Mars radius R_M and local proton gyroradius R_P, respectively. The thickness of HFAs around Mars is from hundreds to tens of thousands of kilometers. On average, the spatial size of HFAs is about 2.9 ± 2.2 R_M. The most probable value is 1–2 R_M. Another significant unit of thickness is the local proton gyroradius R_P, calculated using the magnetic field magnitude and ion temperature inside the core region of HFAs. The spatial size of HFAs ranges from several to tens of R_P. The average thickness of HFAs is 28 R_P, and the occurrence rate of HFAs decreases as the thickness increases.

4.3 Magnetic Geometry

HFAs are ubiquitously characterized as magnetic depression structures, distinguished by a significant decrease in the magnetic field magnitude relative to the ambient IMF. Figure 4 presents the averaged IMF conditions and the magnetic depression manifested by HFAs. As shown in Figure 4a, B_{sw}, which is the magnitude of IMF outside of HFAs, is mainly in the range [1, 4] nT. The averaged B_{sw} is quantified at 2.6 nT, notably exceeding the typical IMF magnitude of 1.9 nT (Liu D et al., 2021). Figure 4b displays the jump in IMF magnitude $\Delta B = |\boldsymbol{B}_{pre}| - |\boldsymbol{B}_{post}|$, where $\boldsymbol{B}_{pre}$ and $\boldsymbol{B}_{post}$ are the ambient IMF preceding and succeeding an HFA event, respectively. While for the majority of events, $|\boldsymbol{B}_{pre}|$ and $|\boldsymbol{B}_{post}|$ are comparable, approximately 10% of the observations exhibit a discrepancy in ΔB that exceeds 1.0 nT. Compared with the ambient IMF, the ratio of B_{min}/B_{sw}, where B_{min} corresponds to the minimum

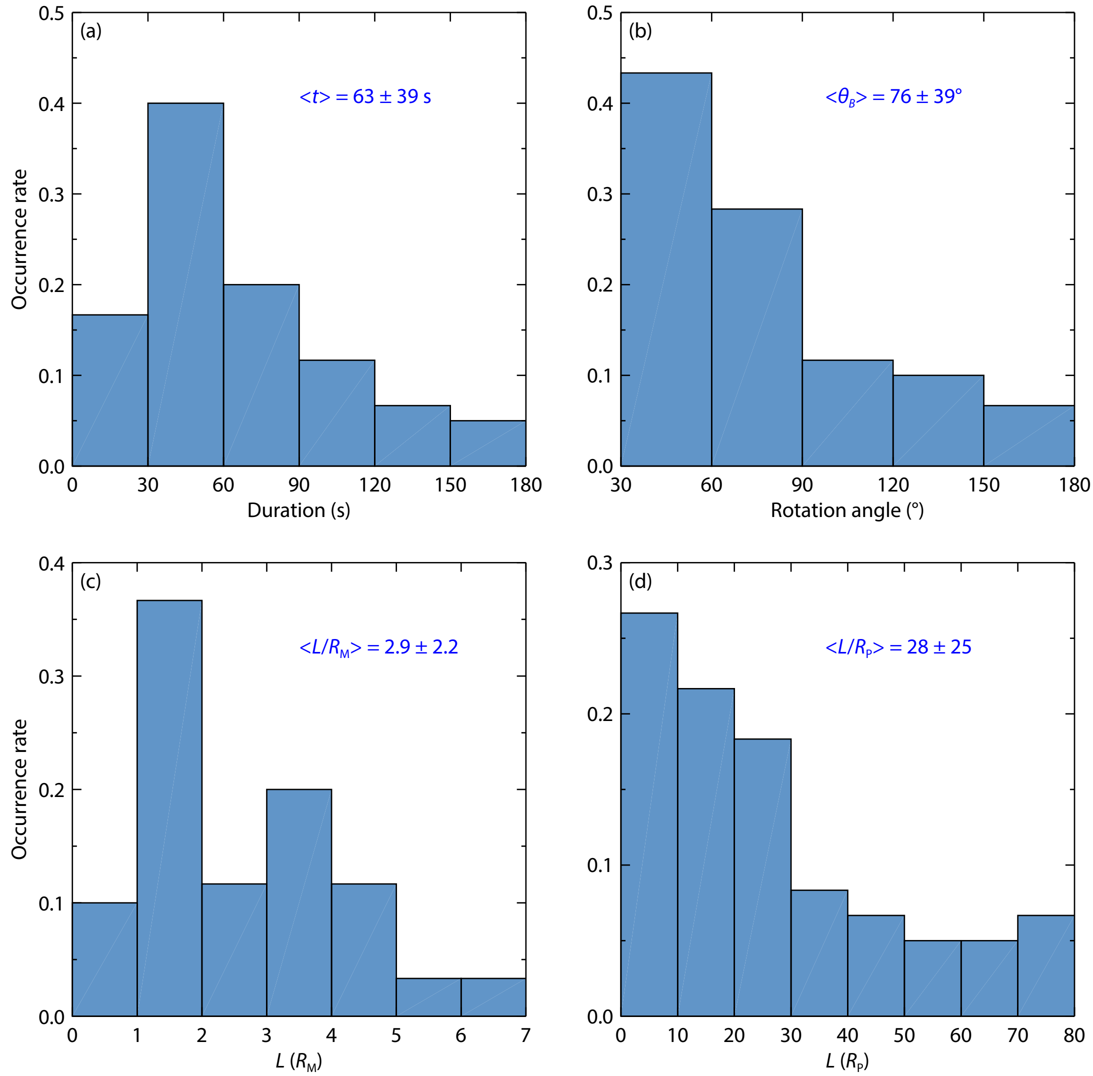

Figure 3. The time duration, rotation angle (L), and size of HFA events around Mars. (a) The duration of Martian HFAs; (b) the rotation angle of the magnetic field across HFA events; (c) the size of Martian HFAs normalized by Martian radius R_M; and (d) the size of Martian HFAs normalized by local proton gyroradii R_P. The average value of each parameter is shown by the dark blue fonts in the top right-hand corner of each image.

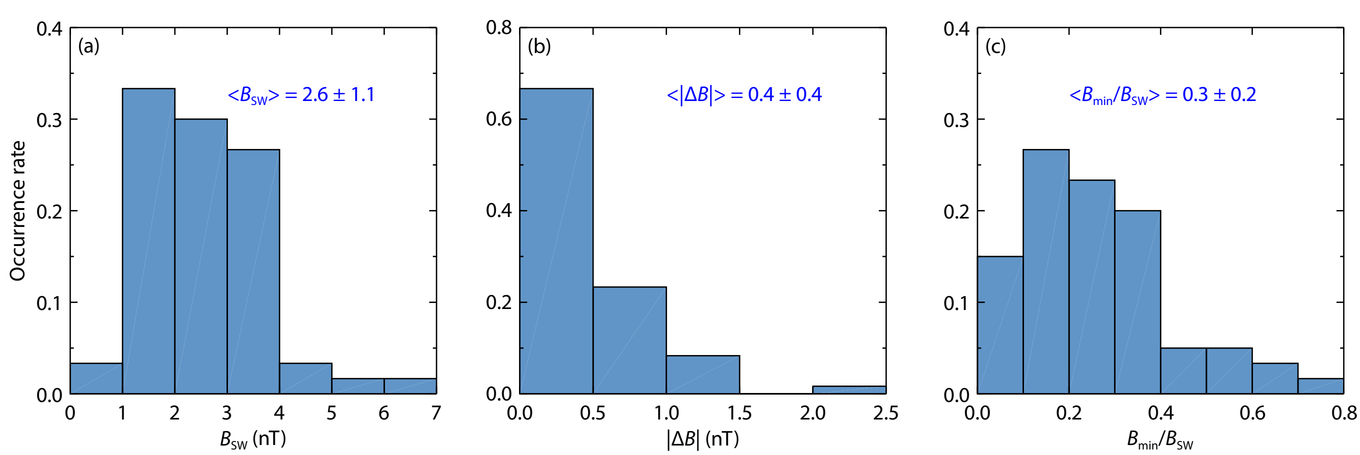

Figure 4. The upstream interplanetary magnetic field (IMF) associated with HFAs around Mars. (a) The magnitude of IMF; (b) the change of IMF magnitude across the HFA event; (c) the size of Martian HFAs in units of Martian radius R_M; and (d) the depth B_{min}/B_{sw} of Martian HFAs. The average value of each parameter is shown by the dark blue fonts in the top right-hand corner of each image.

magnetic field magnitude within the HFA, consistently remains below 0.8. For most events, this ratio is notably lower than 0.4, with an average value of B_{min}/B_{sw} ~0.3.

A toward motional electric field pointing to the corresponding HFA is believed to play an important role in the formation of the HFA (e.g., Thomas et al., 1991; Lin Y, 2002). Schwartz et al. (2000) have already confirmed that the motional electric field $\boldsymbol{E}$ points toward the terrestrial HFAs on at least one side of the associated interplanetary current sheets. Based on the magnetic field and solar wind velocity before and after HFAs, we can calculate the motional electric field $\boldsymbol{E} = -\boldsymbol{V} \times \boldsymbol{B}$, and further check angles between the current normal $\boldsymbol{n}$ and $\boldsymbol{E}$ at the region before and after the Martian HFAs, respectively. There are 78.3% of Martian HFA events that satisfied the requirement that the toward $\boldsymbol{E}$ exists at one side of the HFA at least; 46.7% of HFAs are associated with the toward $\boldsymbol{E}$ at two sides. Hence, the toward motion electric field condition could be also adequate for the formation of Martian HFAs.

4.4 Ion Parameters Associated with HFAs

In the solar wind, more than 90% of ions are protons. The number density of the heavy ions is 2–3 orders lower than that of protons for HFA events. Therefore, ion data obtained from SWIA are used in our statistical work.

Figure 5 shows histograms of the bulk velocity associated with HFAs. In Figure 5a, it can be seen that 90% of events exhibit speeds exceeding 350 km/s, while 65% of events are faster than 400 km/s. On average, the solar wind speed V_{sw} outside of HFAs is 454±89 km/s. A peak of around 500 km/s in this distribution is also notable. Using 5-years of data sets from MAVEN, Liu D et al. (2021) find the average solar wind speed near Mars is 369 km/s. Therefore, the Martian HFAs are always associated with a higher solar wind speed V_{sw}. The speed jump $|\Delta V|$ of the solar wind before and after HFAs in Figure 5b is only 16 ± 13 km/s. Additionally, as the amplitude of the speed jumps increase, the occurrence rate of HFAs decrease. This suggests a minimal variability in the ambient solar wind speed across the HFA boundaries.

A key feature of HFAs is the reduction of bulk velocity within their core regions. Accompanying the magnetic depression, HFAs are invariably marked by a deceleration in the bulk velocity along the Sun–Mars direction. As illustrated in Figure 5c, the ratio of the minimum solar wind speed inside the HFA (V_{min}) to the ambient solar wind speed V_{sw} is determined to be 0.8 ± 0.1. For the majority of events, this ratio varies from 0.60 to 0.95. Compared with the value of $|\Delta V|$ shown in Figure 5b, the deceleration inside HFAs is obvious.

Figure 6 displays variations of ion density associated with HFAs. The ion density of solar wind outside of HFAs (N_{sw}) is typically less than 6.0 cm^{-3}, with the average ion density quantified at 2.6 ± 2.0 cm^{-3}. The jumps in ion number density between the period before and after HFAs ($|\Delta N|$) are relatively small, with over 70% of the events exhibiting a $|\Delta N|$ less than 0.2 cm^{-3}. Within the core regions of HFAs, the ion density can drop to a very low level. Amongst the set of 60 events analyzed, the ion density in the core region (N_{core}) decreases to less than 0.7 times the background values. Statistically, the average ratio of N_{core}/N_{sw} is only 0.2. Moreover, a significant subset, comprising 55% of the events, shows an even more pronounced depletion, with N_{core}/N_{sw} ratios below 0.1. We also check ion number density in the compression regions of HFAs. The maximum ion density N_{com} encountered within the dual compression regions of HFAs is examined. It can be seen in Figure 6d that N_{com}/N_{sw} varies from 1.0 to 4.5, and the average ratio of N_{com}/N_{sw} is 2.3. This compression ratio demonstrates that the hot core of HFAs can effectively compress the ambient plasma. There are only a few HFA events with recognizable heavy ion fluxes. In these events, the density ratio of heavy ion and hydrogen ion in the HFA core region decreases significantly compared with the surrounding solar wind. This also indicates that heavy ions originating from Mars may not play a significant role in the HFA formation.

Figure 7 displays variations of solar wind dynamic pressure associated with HFAs. The solar wind dynamic pressures outside of HFAs (P_{sw}) are characterized by a mean value of 0.8 nPa, with half of observed events clustering in the range 0.5–1.0 nPa. In most HFA events, P_{sw} exhibit few changes between the periods before and

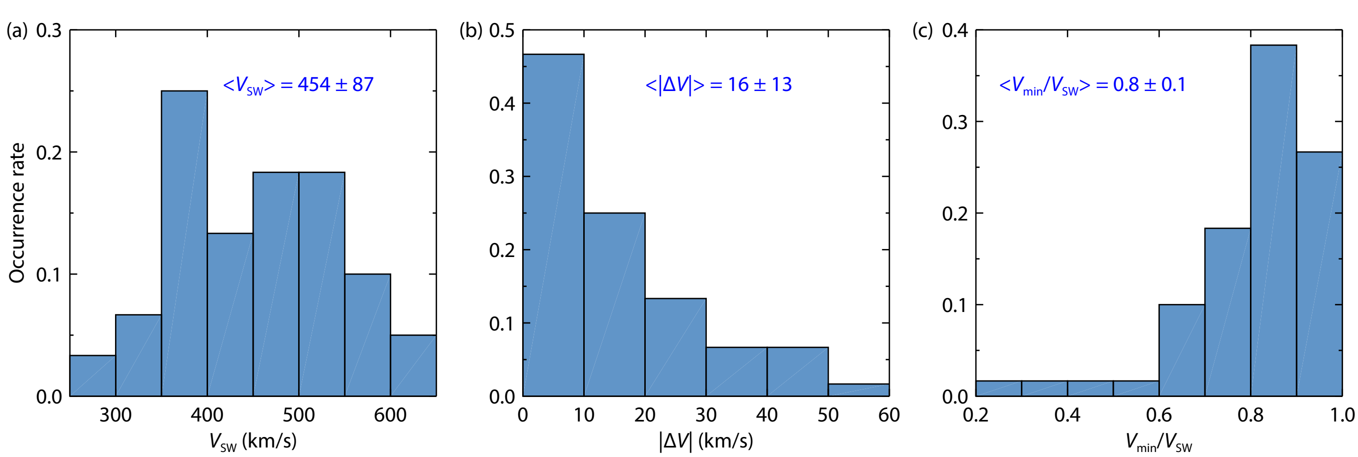

Figure 5. The averaged solar wind velocity on both sides of HFA events. (a) The speed of solar wind associated with HFAs; (b) the change of solar wind speed across the HFA event; and (c) the decrease of the bulk flow speed inside the core region of HFAs. The average value of each parameter is shown by the dark blue fonts in the top right-hand corner of each image.

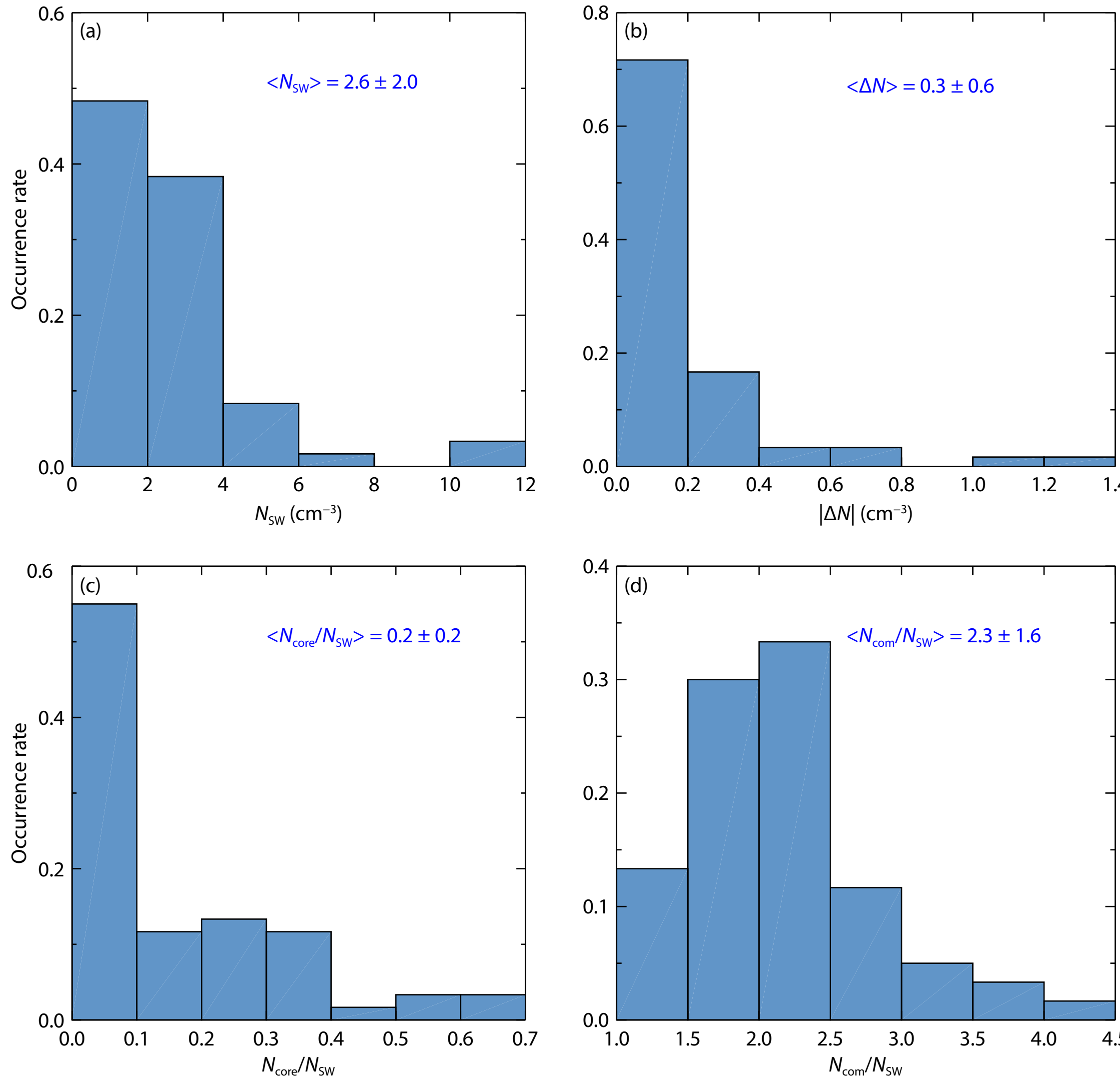

Figure 6. The averaged solar wind number density on both sides of HFA events. (a) The number density of solar wind protons associated with HFAs; (b) the change of proton number density across the HFA event; (c) the decrease of the proton number density inside the core region of HFAs; and (d) the increase of the proton number density inside the compression region of HFAs. The average value of each parameter is shown by the dark blue fonts in the top right-hand corner of each image.

after an HFA event. As shown in Figure 7b, a change in $|\Delta P|$ only has a mean value 0.1 nPa, with most of events with a $|\Delta P|$ below 0.1 nPa. Though the solar wind dynamic pressure outside of HFAs persists essentially unchanged, the HFAs can cause sudden perturbations in the dynamic pressure. Figure 7c and d show variations of dynamic pressure in the core (P_{core}) and compression regions (P_{com}) of HFAs, respectively. It can be noted that P_{core} consistently remains below 0.5 times P_{sw}. The average ratio of P_{core}/P_{sw} is only 0.1. However, within the compression regions, P_{com} is always several times higher than P_{sw}. The average ratio of P_{com}/P_{sw} is 2.3. It means that HFAs can lead to an order of magnitude change in solar wind dynamic pressure within mere seconds.

5. Discussion

5.1 The Comparison of Martian and Terrestrial HFAs

Previous statistical analysis of the MAVEN datasets with the same time interval has already pointed out that the solar wind in the region upstream of the Martian bow shock has a magnitude of IMF ~1.87 nT, V_{sw} ~369 km/s, N_{sw} ~ 1.40 cm^{-3}, and P_{sw} ~0.39 nPa (Liu D et al., 2021). In our study, the magnitude of IMF outside of HFAs is mainly in the range of 1–4 nT, with a mean $\boldsymbol{B}_{sw}$ of ~2.6 nT. The IMF strength has no obvious difference. However, ion parameters of the solar wind outside of HFAs manifest as V_{sw} ~454 km/s, N_{sw} ~2.6 cm^{-3}, and P_{sw} ~0.8 nPa. Thus, 78.3% (47 events) of Martian HFA events are associated with a number density higher than the typical value N_{sw} ~1.40 cm^{-3}. Martian HFAs occur most preferentially with faster solar wind, and 81.7% (49 events) of HFA events occur at speeds higher than V_{sw} ~369 km/s. Therefore, they are usually more prevalent when the ambient solar wind dynamic pressure is higher. Facskó et al. (2009) find the solar wind dynamic pressure outside of HFAs are almost equal to the average value at 1 AU. Hence, the solar wind density outside of HFAs has a relatively lower value. However, Martian HFAs are always formed with higher dynamic pressure and larger density of solar wind than the average value of solar wind upstream of Martian bow shock. But

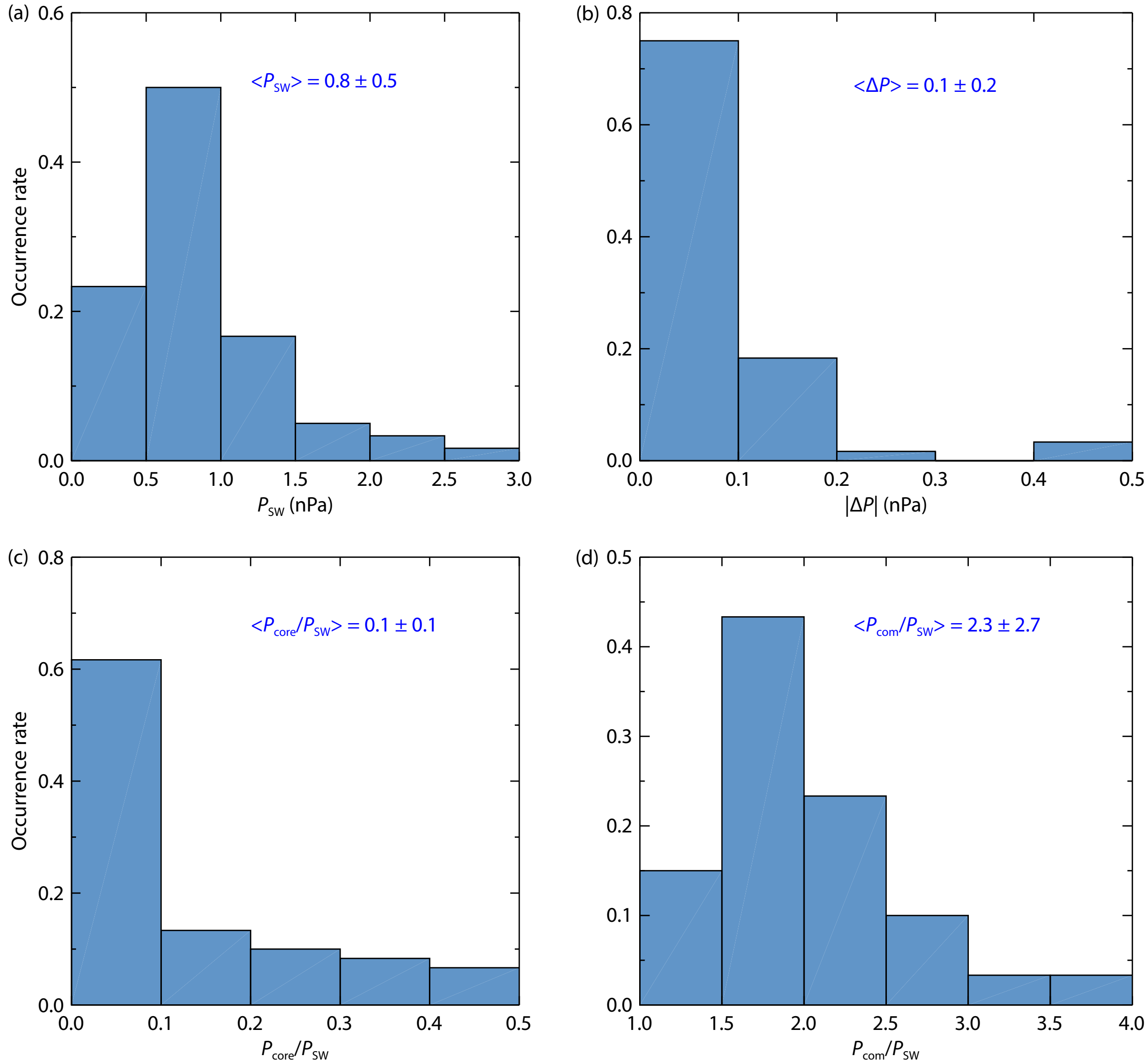

Figure 7. The averaged solar wind dynamic pressure on both sides of HFA events. (a) The dynamic pressure of solar wind associated with HFAs; (b) the change of dynamic pressure across the HFA event; (c) the decrease of the dynamic pressure inside the core region of HFAs; and (d) the increase of the dynamic pressure inside the compression region of HFAs. The average value of each parameter is shown by the dark blue fonts in the top right-hand corner of each image.

the role of the high solar wind dynamic pressure and density in the formation of HFAs seems to be uncertain. In our opinion, this difference is partly determined by the particular features of the two planets. Unlike Earth, the exosphere of Mars can extend for many Martian radii (e.g., Chaffin et al., 2015). Martian particles in the exospheres can be ionized, accelerated by the solar wind motional electric field, and in turn slow down the solar wind. Before the interaction of solar wind and bow shock, the solar wind has already undergone a pronounced deceleration (Zhang TL et al., 1997). Therefore, compared to low-density solar wind, high-density solar wind is more likely to maintain high speeds when interacting with the bow shock. Hence, Martian HFAs typically occur in high-density solar wind, which is also characterized by high dynamic pressure. Of course, the statistical works on HFAs around another planet, or three-dimensional hybrid simulations, may provide a new way to understand this problem.

HFAs are considered to be formed when an interplanetary discontinuity interacts with a planetary bow shock (e.g., Thomas et al., 1991; Lin Y, 2002). The motional electric field $\boldsymbol{E}$ pointing towards this discontinuity at both sides (or at least at one side), can trap the solar wind particles reflected by the Martian bow shock within this discontinuity. Instability caused by the interaction between the incident solar wind particles and the reflected particles can then lead to heating of the interplanetary discontinuity, resulting in high thermal pressure. At last, this HFA can expand and drive compression regions at its two sides. There are plenty of works relating to the features and formation of terrestrial HFAs (e.g., Schwartz et al., 2000; Facskó et al., 2009). Terrestrial HFAs typically exhibit a magnetic field rotation angle of 70° (Facskó et al., 2009). On average, the magnetic field across Martian HFAs rotates at 76°, which is similar to the results of terrestrial HFAs. There is also a requirement that the motional electric field $\boldsymbol{E}$, calculated by $\boldsymbol{E} = -\boldsymbol{V}_{sw} \times \boldsymbol{B}$, should point toward the current sheet on at least one side. Such a requirement is always satisfied in terrestrial HFA events. In this study, 78.3% of Martian HFA events also feature an

E pointed to the current sheet at one or two sides. Furthermore, an essential condition of terrestrial HFA formation is considered to be a larger solar wind velocity, typically exceeding the average by over 100 km/s (Facskó et al., 2009). Congruent with terrestrial observations, our study reveals that Martian HFAs are also correlated with a high solar wind velocity. The solar wind particles are reflected to return to the upstream region of the planetary bow shock, with a similar solar wind speed, but in opposite direction (Thomas et al., 1991; Lin Y, 2002). Therefore, the high solar wind speed could result in more energy of the reflected ion beam. This is a benefit to the formation of HFAs, whether around Earth or Mars. These findings are mirrored in the results of the present study into Martian HFAs, reinforcing the hypothesis that interactions between solar wind current sheet and bow shock serve as the foundational mechanism for HFA production in both terrestrial and Martian environments. A schematic of the formation conditions of an HFA around Mars is shown in Figure 8, based on previous works (Schwartz et al., 2000; Collinson et al., 2012) in addition to our study. This similarity in HFA generation processes across distinct planetary settings underscores the universality of certain physical principles governing plasma interactions within the solar system.

Additionally, previous studies of HFAs around Earth have shown effective acceleration of electrons associated with these structures via magnetic reconnection (e.g., Liu TZ et al., 2020a). We also find the enhancement of energetic electron flux inside of Martian HFAs with energies ranging from 100 eV to 1000 eV, such as event 19 in Table 1. Electron acceleration inside of Martian HFAs is an important question to solve in the future.

5.2 The Probable Effect of HFAs on Martian Ionosphere and Induced Magnetosphere

Due to the lack of simultaneous observations of a Martian HFA, Martian induced magnetosphere boundary (IMB) and ionopause, we are unable to directly investigate IMB and ionopause perturbations induced by HFAs. Collinson et al. (2015) employed a simple static Newtonian pressure equilibrium model to estimate the displacements of the ionopause location R_i from its nominal radial distance R_r:

$$R_i - R_r = -H \ln \frac{P_i}{P_r}, \quad (1)$$

where P_i, P_r and H are the total pressure inside the HFA, pressure outside in the solar wind and the radial height of Martian ionopause (H = 40 km, as shown in Withers, 2009), respectively. It should be noted that the simple model expressed by Equation (2) can also be used to estimate the change of locations of the Martian IMB. In our HFA event on October 1, 2018, the pressure variations associated with this HFA can cause the height of the ionopause to increase by 160 km. Assuming the solar wind dynamic pressure as the dominant component of the total pressure in the solar wind, $-H\ln\frac{P_i}{P_r}$ should be 80 km, which are calculated by the average value. These findings demonstrate the potential of HFAs to significantly influence the Martian topside ionosphere, possibly leading to wider effects.

Edberg et al. (2009) used the correlation analysis method to estimate the influence of solar wind dynamic pressure on the location of the IMB. Their statistical results revealed the radial distance R_{IMB} of the IMB as a function of upstream solar wind dynamic pressure P_{sw}, which can be represented as:

$$R_{\mathrm{IMB}} = 0.21 \times 0.18^{P_{\mathrm{sw}}} + 1.34. \quad (2)$$

By substituting the variations of P_{sw} associated with HFAs, as depicted in Figure 8 of our study into Equation (2), it can be seen that the Martian HFAs lead to a change in R_{IMB} of about 0.12 Martian radius. Such a pronounced displacement occurring in only tens of seconds may lead to some strong oscillations or waves on the surface of the IMB, thereby underscoring the dynamical implications of HFAs on the Martian space environment. We should note however that the response of the induced magnetosphere and ionosphere to HFAs is a complex process, accompanied by boundary layer deformations and wave excitations. A suitable approach would be to employ global numerical simulations.

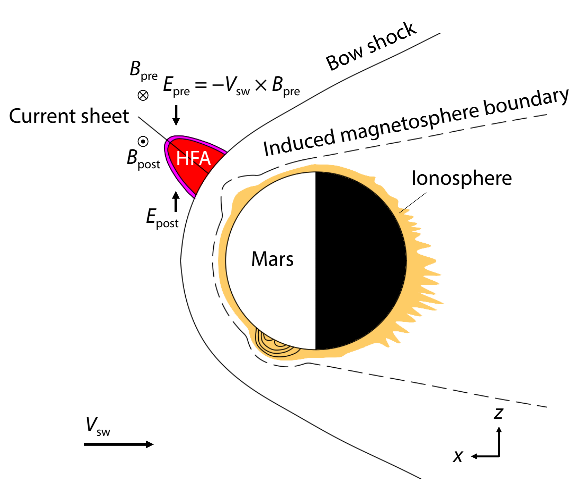

Figure 8. A schematic of the formation conditions of a hot flow anomaly around Mars, which is based on previous works (Schwartz et al., 2000; Collinson et al., 2012) and our study.

5.3 The Thickness of HFAs

The determinants influencing the size of HFAs are still not entirely clear. In our study, we find that the size of Martian HFAs vary from less than one up to several R_{M}, with the average size of HFAs being 2.9 R_{M}. Shuvalov et al. (2019) conducted an analysis of 19 manually selected Martian HFA events, documenting their sizes in the range of 0.2 to ~10 R_{M}, which is consistent with our results. Previous statistical results have shown the typical size of HFAs from Mercury (Uritsky et al., 2014), Venus (Collinson et al., 2014), Earth (e.g., Facskó et al., 2009), Jupiter (Valek et al., 2017) and Saturn (Master et al., 2009) are all within a range of less than one up to several radii of the corresponding planet. This consistency suggests that the spatial size of HFAs might be fundamentally governed by the size of the respective planetary bow shocks.

Nonetheless, when expressed in terms of local proton gyroradii, the characteristic sizes of HFAs exhibit distinct variances around different planets in our solar system. The typical sizes of HFAs in unit of local proton gyroradii are on the order of 200 gyroradii for

Earth (e.g., Facskó et al., 2009), 28 gyroradii for Mars (this study), and 9 gyroradii for Saturn (Master et al., 2009). This trend implies that the size of HFAs normalized by local proton gyroradii gradually decreases with an increase in heliocentric distance. One possible reason is that the thickness of interplanetary current sheets normalized by proton gyroradii also decreases during their propagation. The thickness of solar wind current sheets decreases radially by a factor of 50 from 0.3 to 19 AU (Soding et al., 2001). The decrease in current sheet thickness may consequently serve as a contributing factor to the observed reduction in HFA sizes.

6. Summary

Through a comprehensive analysis of magnetic field and ion measurements from MAVEN collected between October 10, 2014, and December 31, 2020, we have examined 60 Martian HFA events situated upstream of the Martian bow shock. Our results indicate that Martian HFAs share the following properties:

(1) Martian HFAs are common transient structures, and their distributions exhibit no special pattern upstream of the Martian bow shock.
(2) The duration of Martian HFA events extends from tens of seconds to 3 minutes. The average duration is 63±39 s.
(3) On average, the thickness of HFAs, estimated along the normal direction of the associated discontinuity, is about 2.9±2.2 R_M.
(4) Consistent with terrestrial HFAs, Martian HFAs are predominantly detected when the solar wind speed is much higher than the typical value of 369 km/s.
(5) On average, the ratio of ion density in the core region of Martian HFAs to the ion density in the ambient solar wind is 0.2, with over half of the events featuring ratios of below 0.1, revealing a pronounced density depletion within these anomalies.
(6) HFAs can lead to an order of magnitude change in solar wind dynamic pressure in only tens of seconds, which may strongly influence the heights of Martian IMB and ionopause.

Based on these properties, a schematic of Martian HFAs is shown in Figure 8. Our study suggests that HFAs around Mars could be common structures upstream of the bow shock of unmagnetized planets as well, though their occurrence rate still requires further investigation. The formation mechanism of Martian HFAs appears to be same as for terrestrial HFAs, and the planetary heavy ions seem not to play a key role during the formation of HFAs. These transient structures with strong dynamic pressure perturbations may drive significant motions in the induced magnetosphere and ionosphere of Mars. But how HFAs affect the interactions between the solar wind and Mars remains an open question for future global simulations or multiple spacecraft measurements, e.g., the conjunction measurements of MAVEN and Tianwen-1 (Wan WX et al., 2020).

Acknowledgements

We acknowledge the entire MAVEN team and instrument leaders for high quality data and convenient access. The MAVEN data are publicly available through the Planetary Plasma Interactions. All data presented in the figures are publicly available on the Planetary Data System (https://pds.nasa.gov). We thank Dr. Yufei Hao for his kind suggestions. We thank ISSI/ISSJ-BJ through ISSI International Team projects, 'Multi-Scale Magnetosphere−Ionosphere−Thermosphere Interaction' and 'Impact of mesoscale upstream transients on the near-Earth environment'. This work in China was supported by NSFC grants 42274219, 42330207, 42374213 and 42130204; Shenzhen Key Laboratory Launching Project (No. ZDSYS20210702140800001); Mingyu Wu was supported by Frontier Science Center of matter behave in space environment. We would like to acknowledge the support of the National Key Research and Development Program of China (No. 2022YFA1604600).

References

Axford, W. I. (1962). The interaction between the solar wind and the Earth's magnetosphere. *J. Geophys. Res.*, *67*(10), 3791–3796. https://doi.org/10.1029/JZ067i010p03791

Chaffin, M. S., Chaufray, J. Y., Deighan, J., Schneider, N. M., McClintock, W. E., Stewart, A. I. F., Thiemann, E., Clarke, J. T., Holsclaw, G. M., … Jakosky, B. M. (2015). Three-dimensional structure in the Mars H corona revealed by IUVS on MAVEN. *Geophys. Res. Lett.*, *42*(21), 9001–9008. https://doi.org/10.1002/2015GL065287

Collinson, G., Halekas, J., Grebowsky, J., Connerney, J., Mitchell, D., Espley, J., Dibraccio, G., Mazelle, C., Sauvaud, J. A., … Jakosky, B. (2015). A hot flow anomaly at Mars. *Geophys. Res. Lett.*, *42*(21), 9121–9127. https://doi.org/10.1002/2015GL065079

Collinson, G., Sibeck, D., Omidi, N., Grebowsky, J., Halekas, J., Mitchell, D., Espley, J., Zhang, T. L., Persson, M., … Jakosky, B. (2017). Spontaneous hot flow anomalies at Mars and Venus. *J. Geophys. Res.: Space Phys.*, *122*(10), 9910–9923. https://doi.org/10.1002/2017JA024196

Collinson, G. A., Sibeck, D. G., Masters, A., Shane, N., Slavin, J. A., Coates, A. J., Zhang, T. L., Sarantos, M., Boardsen, S., … Barabash, S. (2012). Hot flow anomalies at Venus. *J. Geophys. Res.: Space Phys.*, *117*(A4), A04204. https://doi.org/10.1029/2011JA017277

Collinson, G. A., Sibeck, D. G., Masters A., Shane, N., Zhang, T. L., Fedorov, A., Barabash, S., Coates, A. J., Moore, T. E., … Sarantos, M. (2014). A survey of hot flow anomalies at Venus. *J. Geophys. Res.: Space Phys.*, *119*(2), 978–991. https://doi.org/10.1002/2013JA018863

Connerney, J. E. P., Espley, J., Lawton, P., Murphy, S., Odom, J., Oliversen, R., and Sheppard, D. (2015). The MAVEN magnetic field investigation. *Space Sci. Rev.*, *195*(1), 257–291. https://doi.org/10.1007/s11214-015-0169-4

Dubinin, E., Sauer, K., Delva, M., and Tanaka, T. (1998). The IMF control of the Martian bow shock and plasma flow in the magnetosheath. Predictions of 3-D simulations and observations. *Earth, Planets Space, 50*(10), 873–882. https://doi.org/10.1186/BF03352181

Eastwood, J. P., Lucek, E. A., Mazelle, C., Meziane, K., Narita, Y., Pickett, J., and Treumann, R. A. (2005). The foreshock. *Space Sci. Rev.*, *118*(1), 41–94. https://doi.org/10.1007/s11214-005-3824-3

Edberg, N. J. T., Brain, D. A., Lester, M., Cowley, S. W. H., Modolo, R., Fränz, M., and Barabash, S. (2009). Plasma boundary variability at Mars as observed by Mars Global Surveyor and Mars Express. *Ann. Geophys.*, *27*(9), 3537–3550. https://doi.org/10.5194/angeo-27-3537-2009

Facskó, G., Németh, Z., Erdős, G., Kis, A., and Dandouras, I. (2009). A global study of hot flow anomalies using Cluster multi-spacecraft measurements. *Ann. Geophys.*, *27*(5), 2057–2076. https://doi.org/10.5194/angeo-27-2057-2009

Gruesbeck, J. R., Espley, J. R., Connerney, J. E. P., DiBraccio, G. A., Soobiah, Y. I., Brain, D., Mazelle, C., Dann, J., Halekas, J., and Mitchell, D. L. (2018). The three-dimensional bow shock of Mars as observed by MAVEN. *J. Geophys. Res.: Space Phys.*, *123*(6), 4542–4555. https://doi.org/10.1029/2018JA025366

Halekas, J. S., Taylor, E. R., Dalton, G., Johnson, G., Curtis, D. W., Mcfadden, J. P., Mitchell, D. L., Lin, R. P., and Jakosky, B. M. (2015). The solar wind ion analyzer for MAVEN. *Space Sci. Rev.*, *195*(1), 125–151. https://doi.org/10.1007/s11214-013-0029-z

Halekas, J. S., Ruhunusiri, S., Harada, Y., Collinson, G., Mitchell, D. L., Mazelle, C., Mcfadden, J. P., Connerney, J. E. P., Espley, J. R., … Jakosky, B. M. (2017). Structure, dynamics, and seasonal variability of the Mars-solar wind interaction: MAVEN Solar Wind Ion Analyzer in-flight performance and science results. *J. Geophys. Res.: Space Phys.*, *122*(1), 547–578. https://doi.org

/10.1002/2016JA023167

Jakosky, B. M., Lin, R. P., Grebowsky, J. M., Luhmann, J. G., Mitchell, D. F., Beutelschies, G., Priser, T., Acuna, M., Andersson, L., … Zurek, R. (2015). The *Mars Atmosphere and Volatile Evolution* (MAVEN) mission. *Space Sci. Rev.*, *195*(1), 3–48. https://doi.org/10.1007/s11214-015-0139-x

Lin, Y. (2002). Global hybrid simulation of hot flow anomalies near the bow shock and in the magnetosheath. *Planet. Space Sci.*, *50*(5-6), 577–591. https://doi.org/10.1016/S0032-0633(02)00037-5

Lin, Y., Wang, X. Y. , Sibeck, D. G., Wang, C. P., and Lee, S. H. (2022). Global asymmetries of hot flow anomalies. *Geophys. Res. Lett.*, *49*(4), e2021GL096970. https://doi.org/10.1029/2021GL096970

Liu, D., Rong, Z. J., Gao, J. W., He, J. S., Klinger, L., Dunlop, M. W., Yan, L. M., Fan, K., and Wei, Y. (2021). Statistical properties of solar wind upstream of Mars: MAVEN observations. *Astrophys. J.*, *911*(2), 113. https://doi.org/10.3847/1538-4357/abed50

Liu, T. Z., Lu, S., Turner, D. L., Gingell, I., Angelopoulos, V., Zhang, H., Artemyev, A., and Burch, J. L. (2020a). Magnetospheric Multiscale (MMS) observations of magnetic reconnection in foreshock transients. *J. Geophys. Res.: Space Phys.*, *125*(4), e2020JA027822. https://doi.org/10.1029/2020JA027822

Liu, T. Z., Wang, C. P., Wang, B. Y., Wang, X. Y., Zhang, H., Lin, Y., and Angelopoulos, V. (2020b). ARTEMIS observations of foreshock transients in the midtail foreshock. *Geophys. Res. Lett.*, *47*(21), e2020GL090393. https://doi.org/10.1029/2020GL090393

Masters, A., McAndrews, H. J., Steinberg, J. T., Thomsen, M. F., Arridge, C. S., Dougherty, M. K., Billingham, L., Schwartz, S. J., Sergis, N., … Coates, A. J. (2009). Hot flow anomalies at Saturn's bow shock. *J. Geophys. Res.: Space Phys.*, *114*(A8), A08217. https://doi.org/10.1029/2009JA014112

Mazelle, C., Winterhalter, D., Sauer, K., Trotignon, J. G., Acuña, M. H., Baumgärtel, K., Bertucci, C., Brain, D. A., Brecht, S. H., … Slavin, J. (2004). Bow shock and upstream phenomena at Mars. *Space Sci. Rev.*, *111*(1), 115–181. https://doi.org/10.1023/B:SPAC.0000032717.98679.d0

McFadden, J. P., Kortmann, O., Curtis, D., Dalton, G., Johnson, G., Abiad, R., Sterling, R., Hatch, K., Berg, P., … Jakosky, B. (2015). MAVEN suprathermal and thermal ion compostion (STATIC) instrument. *Space Sci. Rev.*, *195*(1), 199–256. https://doi.org/10.1007/s11214-015-0175-6

Øieroset, M., Mitchell, D. L., Phan, T. D., Lin, R. P., and Acuña, M. H. (2001). Hot diamagnetic cavities upstream of the Martian bow shock. *Geophys. Res. Lett.*, *28*(5), 887–890. https://doi.org/10.1029/2000GL012289

Omidi, N., and Sibeck, D. G. (2007). Formation of hot flow anomalies and solitary shocks. *J. Geophys. Res.: Space Phys.*, *112*(A1), A01203. https://doi.org/10.1029/2006JA011663

Onsager, T. G., Winske, D., and Thomsen, M. F. (1991). Interaction of a finite-length ion beam with a background plasma: Reflected ions at the quasi-parallel bow shock. *J. Geophys. Res.: Space Phys.*, *96*(A2), 1775–1788. https://doi.org/10.1029/90JA02008

Rahmati, A., Larson, D. E., Cravens, T. E., Lillis, R. J., Halekas, J. S., McFadden, J. P., Dunn, P. A., Mitchell, D. L., Thiemann, E. M. B., … Jakosky, B. M. (2017). MAVEN measured oxygen and hydrogen pickup ions: Probing the Martian exosphere and neutral escape. *J. Geophys. Res.: Space Phys.*, *122*(3), 3689–3706. https://doi.org/10.1002/2016JA023371

Russell, C. T., and Hoppe, M. M. (1983). Upstream waves and particles. *Space Sci. Rev.*, *34*(2), 155–172. https://doi.org/10.1007/BF00194624

Schwartz, S. J., Chaloner, C. P., Christiansen, P. J., Coates, A. J., Hall, D. S., Johnstone, A. D., Gough, M. P., Norris, A. J., Rijnbeek, R. P., … Woolliscroft, L. J. C. (1985). An active current sheet in the solar wind. *Nature*, *318*(6043), 269–271. https://doi.org/10.1038/318269a0

Schwartz, S. J., Paschmann, G., Sckopke, N., Bauer, T. M., Dunlop, M., Fazakerley, A. N., and Thomsen, M. F. (2000). Conditions for the formation of hot flow anomalies at Earth's bow shock. *J. Geophys. Res.: Space Phys.*, *105*(A6), 12639–12650. https://doi.org/10.1029/1999JA000320

Shuvalov, S. D., Ermakov, V. N., Zorina, V. O., and Kim, K. I. (2019). Propagation properties of Hot Flow Anomalies at Mars: MAVEN observations. *Planet. Space Sci.*, *179*, 104717. https://doi.org/10.1016/j.pss.2019.104717

Sibeck, D. G., Borodkova, N. L., and Schwartz, S. J. (1999). Comprehensive study of the magnetospheric response to a hot flow anomaly. *J. Geophys. Res.: Space Phys.*, *104*(A3), 4577–4593. https://doi.org/10.1029/1998JA900021

Slavin, J. A., Acuña, M. H., Anderson, B. J., Barabash, S., Benna, M., Boardsen, S. A., Fraenz, M., Gloeckler, G., Gold, R. E., and Zurbuchen, T. H. (2009). MESSENGER and Venus Express observations of the solar wind interaction with Venus. *Geophys. Res. Lett.*, *36*(9), L09106. https://doi.org/10.1029/2009GL037876

Soding, A., Neubauer, F. M., Tsurutani, B. T., Ness, N. F., and Lepping, R. P. (2001). Radial and latitudinal dependencies of discontinuities in the solar wind between 0.3 and 19 AU and $-80°$ and $+10°$. *Ann. Geophys.*, *19*, 667–680. https://doi.org/10.5194/angeo-19-667-2001

Thomas, V. A., Winske, D., Thomsen, M. F., and Onsager, T. G. (1991). Hybrid simulation of the formation of a hot flow anomaly. *J. Geophys. Res.: Space Phys.*, *96*(A7), 11625–11632. https://doi.org/10.1029/91JA01092

Thomsen, M. F., Gosling, J. T., Fuselier, S. A., Bame, S. J., and Russell, C. T. (1986). Hot, diamagnetic cavities upstream from the Earth's bow shock. *J. Geophys. Res.: Space Phys.*, *91*(A3), 2961–2973. https://doi.org/10.1029/JA091iA03p02961

Trotignon, J. G., Mazelle, C., Bertucci, C., and Acuña, M. H. (2006). Martian shock and magnetic pile-up boundary positions and shapes determined from the Phobos 2 and Mars Global Surveyor data sets. *Planet. Space Sci.*, *54*(4), 357–369. https://doi.org/10.1016/j.pss.2006.01.003

Uritsky, V. M., Slavin, J. A., Boardsen, S. A., Sundberg, T., Raines, J. M., Gershman, D. J., Collinson, G., Sibeck, D., Khazanov, G. V., … Korth, H. (2014). Active current sheets and candidate hot flow anomalies upstream of Mercury's bow shock. *J. Geophys. Res.: Space Phys.*, *119*(2), 853–876. https://doi.org/10.1002/2013JA019052

Valek, P. W., Thomsen, M. F., Allegrini, F., Bagenal, F., Bolton, S., Connerney, J., Ebert, R. W., Gladstone, R., Kurth, W. S., … Wilson, R. J. (2017). Hot flow anomaly observed at Jupiter's bow shock. *Geophys. Res. Lett.*, *44*(16), 8107–8112. https://doi.org/10.1002/2017GL073175

Vignes, D., Acuña, M. H., Connerney, J. E. P., Crider, D. H., Rème, H., and Mazelle, C. (2002). Factors controlling the location of the bow shock at Mars. *Geophys. Res. Lett.*, *29*(9), 1328. https://doi.org/10.1029/2001GL014513

Wan, W. X., Wang, C., Li, C. L., Wei, Y., and Liu, J. J. (2020). The payloads of planetary physics research onboard China's First Mars Mission (Tianwen-1). *Earth Planet. Phys.*, *4*(4), 331–332. https://doi.org/10.26464/epp2020052

Wang, M., Xie, L., Lee, L. C., Xu, X. J., Kabin, K., Lu, J. Y., Wang, J., and Li, L. (2020). A 3D parametric Martian bow shock model with the effects of mach number, dynamic pressure, and the interplanetary magnetic field. *Astrophys. J.*, *903*(2), 125. https://doi.org/10.3847/1538-4357/abbc04

Wang, S., Zong, Q. G., and Zhang, H. (2013a). Cluster observations of hot flow anomalies with large flow deflections: 1. Velocity deflections. *J. Geophys. Res.: Space Phys.*, *118*(2), 732–743. https://doi.org/10.1002/jgra.50100

Wang, S., Zong, Q. G., and Zhang, H. (2013b). Cluster observations of hot flow anomalies with large flow deflections: 2. Bow shock geometry at HFA edges. *J. Geophys. Res.: Space Phys.*, *118*(1), 418–433. https://doi.org/10.1029/2012JA018204

Withers, P. (2009). A review of observed variability in the dayside ionosphere of Mars. *Adv. Space Res.*, *44*(3), 277–307. https://doi.org/10.1016/j.asr.2009.04.027

Yamauchi, M., Hara, T., Lundin, R., Dubinin, E., Fedorov, A., Sauvaud, J. A., Frahm, R. A., Ramstad, R., Futaana, Y., … Barabash, S. (2015). Seasonal variation of Martian pick-up ions: Evidence of breathing exosphere. *Planet. Space Sci.*, *119*, 54–61. https://doi.org/10.1016/j.pss.2015.09.013

Zhang, H., Sibeck, D. G., Zong, Q. G., Gary, S. P., Mcfadden, J. P., Larson, D., Glassmeier, K. H., and Angelopoulos, V. (2010). Time history of events and macroscale interactions during substorms observations of a series of hot flow anomaly events. *J. Geophys. Res.: Space Phys.*, *115*(A12), A12235. https://doi.org/10.1029/2009JA015180

Zhang, T. L., Schwingenschun, K., Riedler, W., Kotova, G., Verigin, M., Tatrallyay, M., and Russell, C. T. (1997). Solar wind deceleration at Mars and Earth: A comparison. *Adv. Space Res.*, *20*(2), 133–136, https://doi.org/10.1016/S0273-1177(97)00522-X

Zhang, T. L., Delva, M., Baumjohann, W., Volwerk, M., Russell, C. T., Barabash, S., Balikhin, M., Pope, S., Glassmeier, K. H., and Kudela, K. (2008). Initial Venus Express magnetic field observations of the Venus bow shock location at solar minimum. *Planet. Space Sci.*, *56*(6), 785–789. https://doi.org/10.1016/j.pss.2007.09.012

Zhao, L. L., Zong, Q. G., Zhang, H., and Wang, S. (2015). Case and statistical studies on the evolution of hot flow anomalies. *J. Geophys. Res.: Space Phys.*, *120*(8), 6332–6346. https://doi.org/10.1002/2014JA020862